npj | climate and atmospheric science

www.nature.com/npjclimatsci

ARTICLE OPEN

Check for updates

A super dust storm enhanced by radiative feedback

Yu Chen[1], Siyu Chen[1]✉, Jie Zhou[1], Dan Zhao[1], Hongru Bi[1], Yue Zhang[1], Khan Alam[1,2], Haipeng Yu[3], Yaoxian Yang[3] and Junyan Chen[1]

As the main dust source area in East Asia, the Gobi Desert (GD) exerts critical impacts on the radiation budget in downstream regions. Dust radiative feedback in the GD on the Mongolian cyclone, however, remains poorly understood. Herein, the dynamic dust source is coupled with the Weather Research and Forecasting model with Chemistry (WRF-Chem) for better dust simulations. Results show that the Mongolian cyclone dominates the dust event in May 2019. Dust radiative feedback results in downward momentum transport and cools northeast of Mongolia by affecting zonal winds and temperature advection. Lower-troposphere cooling and upper-atmosphere warming change the atmospheric vertical structure and enhance baroclinicity. Further, cold air deeply descends into the bottom of the warm air in a wedge shape and promotes the ascension of warm air to enhance the Mongolian cyclone. The strong dust is maintained and continues to cause high dust concentrations in northern China via westerlies. This study explores how dust radiative feedback over the GD can intensify the Mongolian cyclone and provides a scientific reference for related studies.

npj Climate and Atmospheric Science (2023)6:90 ; https://doi.org/10.1038/s41612-023-00418-y

INTRODUCTION

Dust is the main component of atmospheric aerosols, accounting for 75% of the global aerosol mass loading and 25% of the global aerosol optical depth (AOD)[1]. It is mainly caused by aeolian erosion over drylands and affects the energy budget of the Earth–atmosphere system and hydrological cycle through direct and indirect effects[2–5]. Moreover, dust particles can be enriched with germs[6], organics[7], and heavy metals[8], posing a serious threat to human health and socioeconomic activities by affecting air quality[9–11]. After a long-distance transport, dust particles are deposited on the ocean surface, affecting the generation of biogenic aerosols over the ocean and changing the marine biogeochemical cycle and biological productivity[12,13].

Aerosol–radiation interaction considerably impacts climate changes, weather processes, and air quality[14]. On the one hand, changes in meteorological processes can alter the transport and spatial distribution of dust[15,16]. On the other hand, dust affects the atmospheric system and air quality through radiative feedback[17]. Dust direct radiative forcing values for the Taklimakan Desert (TD) and Gobi Desert (GD) are reported as −3 and −7 W m^{-2} at the top of the atmosphere (TOA), −8 and −10 W m^{-2} at the surface, and +5 and +3 W m^{-2} in the atmosphere[18]. In addition, dust radiative forcing can considerably change atmospheric stratification and baroclinicity[19]. GD dust enhances the anthropogenic aerosol pollution in eastern China by changing the meteorological field[20]. The dust-induced pressure disturbance prompts secondary circulation, which reduces the wind speed at the low atmospheric level over the dust source region and enhances the wind speed at the downstream regions, resulting in dust reduction and enhancement in the upper source region and downstream regions, respectively[21].

Located at the border between China and Mongolia, the GD is an important source of dust in East Asia[22–24]. As a typical plateau desert, the GD is characterized by a low average annual temperature and drastic temperature changes[25]. Dust storms occur abruptly in this region over wide areas but are short in duration. The dust-event frequency at the China–Mongolia border has shown a gradually increasing trend[26,27], and GD dust is the main source of dust-type air pollution in the inland areas of China, particularly, Beijing–Tianjin–Hebei[28]. GD is characterized by flat terrain, and the entire troposphere is dominated by westerly winds. The combination of special terrain and background winds provides conditions for trans-Pacific eastward transmission of dust to North America[29,30].

Although researchers have consistently discussed the importance of GD's contributions to dust sources in East Asia[28], the effect of GD dust on the weather and climate in this region has been poorly studied. As an important weather system, the Mongolian cyclone can generate strong surface winds that lift surface particles into the atmosphere and then produce severe dust storms[31]. The outbreak of dust storms in East Asia is often closely related to the activity of cold air and the Mongolian cyclone[23,32]. Cyclones with cold air are common in Mongolia, and the GD and TD generate large amounts of dust that is transported to the downstream regions[33]. Moreover, the westerly ridge and East Asian vortex at 500 hPa are key drivers of long-distance dust transport[34,35]. A severe dust event occurred in May 2019 directly affected 168 people in a county in Inner Mongolia, resulting in direct economic losses of 1.004 million RMB[36]. Herein, the May 2019 event is used as a typical case to further explore the relation between Mongolian cyclone and the dust radiative feedback in the GD. We use dynamic dust sources, the Weather Research and Forecasting (WRF) model coupled with Chemistry (WRF-Chem), and satellite retrievals to develop a comprehensive understanding of this event. Further, we explore the mechanism of dust radiative feedback in the GD on enhancing Mongolian cyclone and its continued effect on dust concentrations over downstream regions.

RESULTS

Spatial–temporal dust distribution

MODIS composite image shows that this dust event was closely related to Mongolian cyclone (Fig. 1a). The obvious comma cloud

[1]Key Laboratory for Semi-Arid Climate Change of the Ministry of Education, Lanzhou University, Lanzhou 730000, China. [2]Department of Physics, University of Peshawar, Peshawar 25120, Pakistan. [3]Key Laboratory of Land Surface Process and Climate Change in Cold and Arid Regions, Northwest Institute of Eco-Environment and Resources, Chinese Academy of Sciences, Lanzhou 730000, China. ✉email: chensiyu@lzu.edu.cn

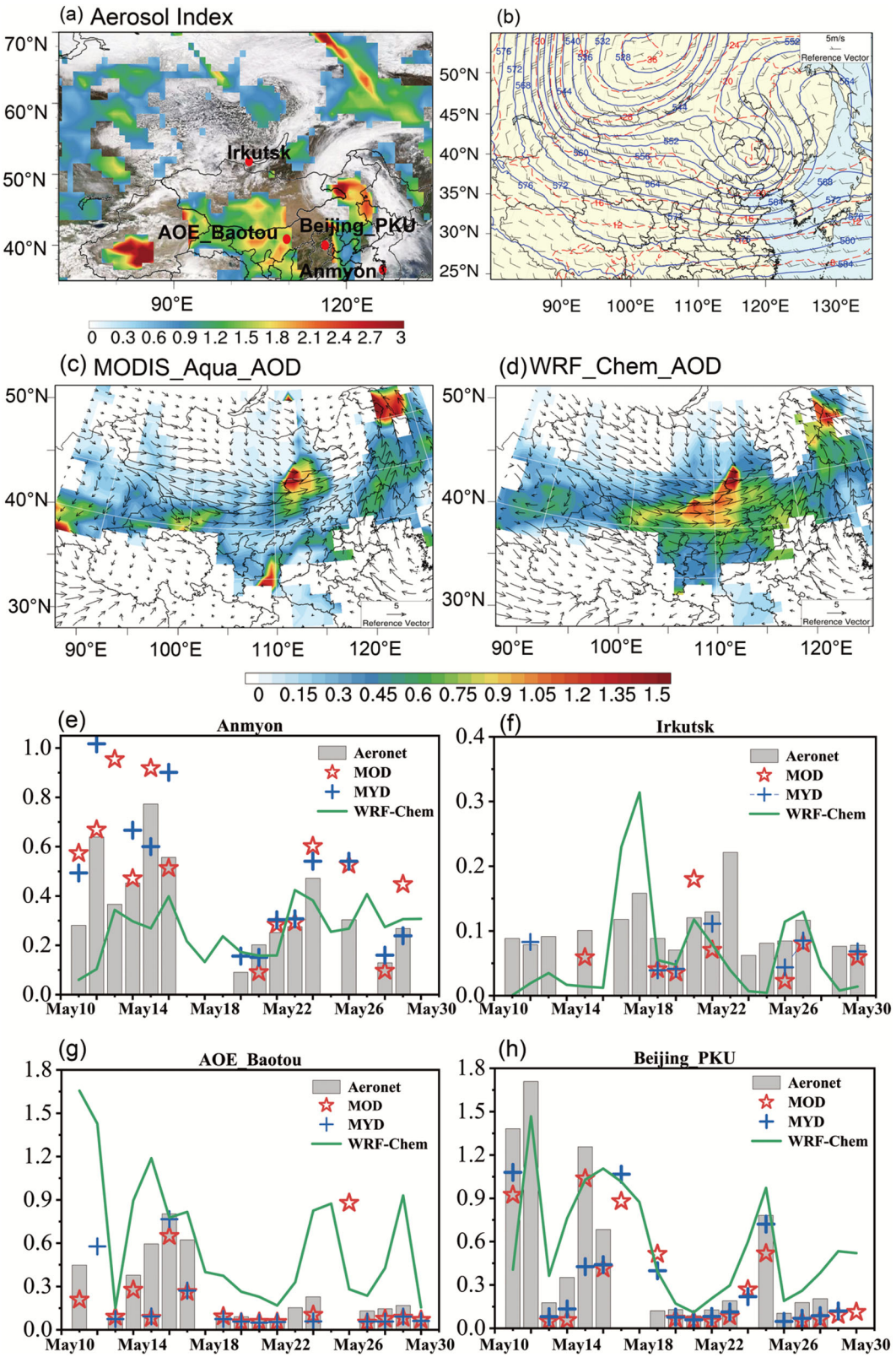

system over northern China in the figure indicates that the Mongolian cyclone enhanced the easterly transport of mid-latitude dust aerosols via atmospheric circulation. At the same time, the simulated weather circulation also captures a deep vortex structure over northern China on May 13, 2019 (Fig. 1b). WRF–Chem effectively captured the maximum MODIS aerosol distribution in central and eastern Inner Mongolia and in northern Heilongjiang, with AOD values up to 1.8 (Fig. 1c, d). There are well-documented evidence for the connection of aerosol index (AI) and aerosol concentrations and optical properties[37]. It is a qualitative

Fig. 1 Model evaluation of AOD spatiotemporal distribution. a MODIS Aqua composite image overlaid by OMI Aerosol Index (AI) on May 13 2019. The red dots indicate the AERONET observation stations including Irkutsk, AOE_Baotou, Beijing_PKU, and Anmyon. **b** Spatial patterns of the geopotential height (blue contour lines; unit: dagpm), temperature (red contour lines; unit: °C), and wind field (vectors; unit: m s^{-1}) at 500 hPa on May 13, 2019, retrieved using WRF-Chem. Spatial distributions of the average AOD based on (**c**) MODIS (MYD08_D3) and (**d**) WRF-Chem simulations are shown for May 11–16, 2019. The wind field at 10 m (vectors; unit: m s^{-1}) was obtained from (**c**) Final Operational Global Analysis (FNL) reanalysis and (**d**) WRF-Chem simulation. Daily variation of AOD from AERONET observations (Aeronet) at four sites (Anmyon (36.539°N, 126.330°E), Irkutsk (51.800°N, 103.087°E), AOE_Baotou (40.852°N, 109.629°E), Beijing_PKU (39.992°N, 116.310°E)) (**e**, **f**, **g**, **h**), MODIS on board Terra (MOD) and Aqua (MYD), and the WRF-Chem model (WRF-Chem) on May 11–30, 2019. The results associated with WRF-Chem are based on the EXP_CTRL experiment.

factor represent aerosol particles suspended in the atmosphere, mainly from desert dust, biomass burning and volcanic ash plumes, and it has already been used to identify dust aerosols[38]. Generally speaking, both OMI AI and WRF–Chem AOD show consistent zonal distribution in Inner Mongolia (Supplementary Fig. 3). The air in northern China was also severely polluted, with the AI peaking at 2.9. The AOD values shifted eastward owing to the lack of MODIS measurement in the main areas of the dust source in the event.

To verify the numerical simulation of dust aerosols based on the WRF–Chem model, the simulated AOD on May 11–16 was evaluated using ground observations. The AOD recorded at Anmyon, Irkutsk, Academy of Optoelectronics (AOE)_Baotou, and Beijing_Peking University (PKU) sites derived from Terra, Aqua, and AERONET data were compared with the WRF–Chem results (Fig. 1). Simulations well reproduced the observed AOD in China. Specifically, Beijing suffered from serious air pollution during this dust event, with AOD values generally >0.5, whereas the WRF-Chem AOD was close to that of MODIS and AERONET (Fig. 1h). Although the simulated AOD in Baotou was overestimated compared with the observations, basic aerosol changes were noted (Fig. 1g). Moreover, the AOD simulations at the Anmyon station and the Irkutsk station were in good agreement with the observations (Fig. 1e, f).

Dust emission in the dust event was concentrated mainly over the GD (Supplementary Fig. 5). The maximum multiday average dust emission flux was as high as 182.1 μg m^{-2} s^{-1}, and a small amount of dust particles was emitted from the TD. In the case of daily dust emission, peaks at 554.2 μg m^{-2} s^{-1} and 264.7 μg m^{-2} s^{-1} were simulated at the same grid (44.58408°N, 99.15584°E) on May 11 and 14, 2019, respectively, and the dust emission area extended eastward to 110°E. The occurrence of dust storms is usually closely associated to the invasion of cold air[29]. Cold air from Siberia is continuously transported to the GD, and the GD dust then affects the area over northeastern Mongolia via the southerly wind (Supplementary Fig. 6). In addition, Supplementary Fig. 6b shows that a weak cyclone was generated over northern Mongolia and the eastern region of Inner Mongolia on May 12, 2019. Mongolian cyclone gradually intensified and peaked on May 13, 2019, and a common cloud system is also found based on the satellite cloud images (Supplementary Fig. 7). The sea level pressure in the center of Mongolian cyclone on May 13 was lower than that on May 12. Moreover, the cyclonic wind field in northern Mongolia gradually dissipated on May 14 (Supplementary Fig. 6d). Therefore, it gradually intensified and peaked on May 13, 2019, and a comma cloud system is also found based on the composite image (Fig. 1a). Mongolian cyclone combined with southward cold air strengthened dust intensity in the dust event. The persistent maintenance of cyclones in central Siberia is conducive to continuous eastward transport of dust aerosols (Supplementary Fig. 6). Therefore, the combination of cold air and Mongolian cyclone promoted larger dust emission and dust loading on May 14 compared that on May 13. Moreover, the temperature field always lags behind the height field at different altitude levels, which is conducive to the development of trough–ridge systems. The large angle between the temperature and height fields in the middle and low atmospheric layers is beneficial for the southward movement of cold air from northern areas, and the transport of cold advection and the powerful cyclone in north of Mongolia enhances the development of dust storms (Supplementary Fig. 8). These phenomena enable the GD dust to continuously affect the downstream regions.

The dust transport flux at 850 hPa was concentrated over Inner Mongolia. With increasing altitude, the dust transport flux moved eastward to North China and Northeast China under westerly jets at 500 hPa (Fig. 2a, b). The spatial distribution of dust transport flux clearly shows that GD dust was transported to northeast of Mongolia, North China, and other downstream areas. Atmospheric uplift between 105°E and 110°E is conducive to the lifting of the dust, and then dust concentrations gradually spreads eastly through westerly winds (Fig. 2c). The GD and TD were the main dust emission areas in the dust event (Supplementary Fig. 5). To explore the relative contributions of dust and their uplifting capacity from these two sources[28], we compared the dust concentrations and dust ratio in the middle and lower troposphere with those in the upper atmosphere (Fig. 2d, e). Specifically, the maximum GD dust concentrations at the middle and low troposphere (3–10 km) was 31.4 μg m^{-3}, whereas that in high atmosphere (8–10 km) was 2.3 μg m^{-3} (Supplementary Fig. 11), with average values of 14.2 μg m^{-3} and of 0.5 μg m^{-3}, respectively. Regarding TD dust, the maximum concentrations was 18.5 μg m^{-3} at the middle and low troposphere while that in the high layer was ~1.5 μg m^{-3}, with average values of 6.4 and 0.2 μg m^{-3}, respectively. The concentrations of GD dust in different layers of the atmosphere and the ratio of the dust concentrations in the upper layer to that in the lower layer (below 3 km) were both greater than those for TD dust. Specifically, the average dust ratios for the GD and TD were 3.88% and 2.97% at 3–10 km and 0.17% and 0.084% at 8–10 km, respectively. The larger dust concentrations and dust ratio for the GD indicate that GD has higher lofting of dust, and the contribution of GD to atmospheric dust concentrations was also greater than that of the TD.

Influence of dust radiative feedback on Mongolian cyclone

Dust affects the regional atmospheric thermal structure through direct radiative forcing, which in turn affects the regional climate[39,40] and dust cycles[41]. The net radiative forcing values of dust at the TOA in North and Northeast China were mainly negative (~−20 W m^{-2}), indicating that dust has a cooling effect in the Earth–atmosphere system in this region. As a typical absorbing aerosol, dust can warm the atmosphere[40], and the net radiative forcing of dust in the atmosphere is mainly positive. The dust layer mainly appeared near 850 hPa, and the regional average dust concentrations reached the maximum at 875 hPa (729.12 μg m^{-3}) (Fig. 3d). The influence of dust radiative feedback on the atmospheric heating rate varied with dust concentrations, and the atmospheric heating rate also reached 0.33 K day^{-1} at 700 hPa.

Owing to the strong scattering and absorption of dust in the atmosphere as well as the influence of clouds, the amount of solar shortwave radiation reaching the surface was reduced. The net radiative forcing and shortwave radiative forcing of dust near the

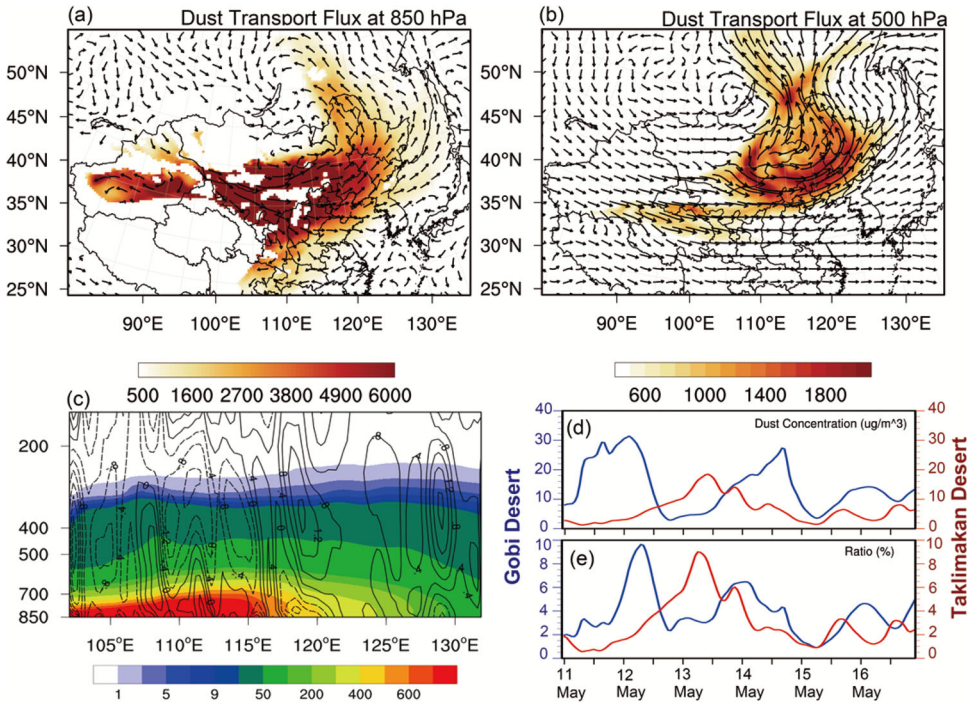

Fig. 2 The basic physical processes in this dust event. Spatial distribution of dust transport flux (color contour, unit: μg m^{-2} s^{-1}) at (**a**) 850 and (**b**) 500 hPa. **c** Average cross sections of dust concentrations (color contour, unit: μg m^{-3}) and vertical speed (contour lines, unit: m s^{-1}) during May 11–16, 2019, over domain 2 (solid and dashed lines represent ascent and descent motions, respectively). **d** Hourly average dust concentrations (unit: μg m^{-3}) over the TD (35–45°N, 85–95°E; red solid line) and GD (35–45°N, 95–110°E; blue solid line) at 3–10 km altitude. **e** Ratio of dust concentrations (%) at 3–10 km against that measured below 3 km during May 11–16, 2019. The results are based on the EXP_CTRL experiment.

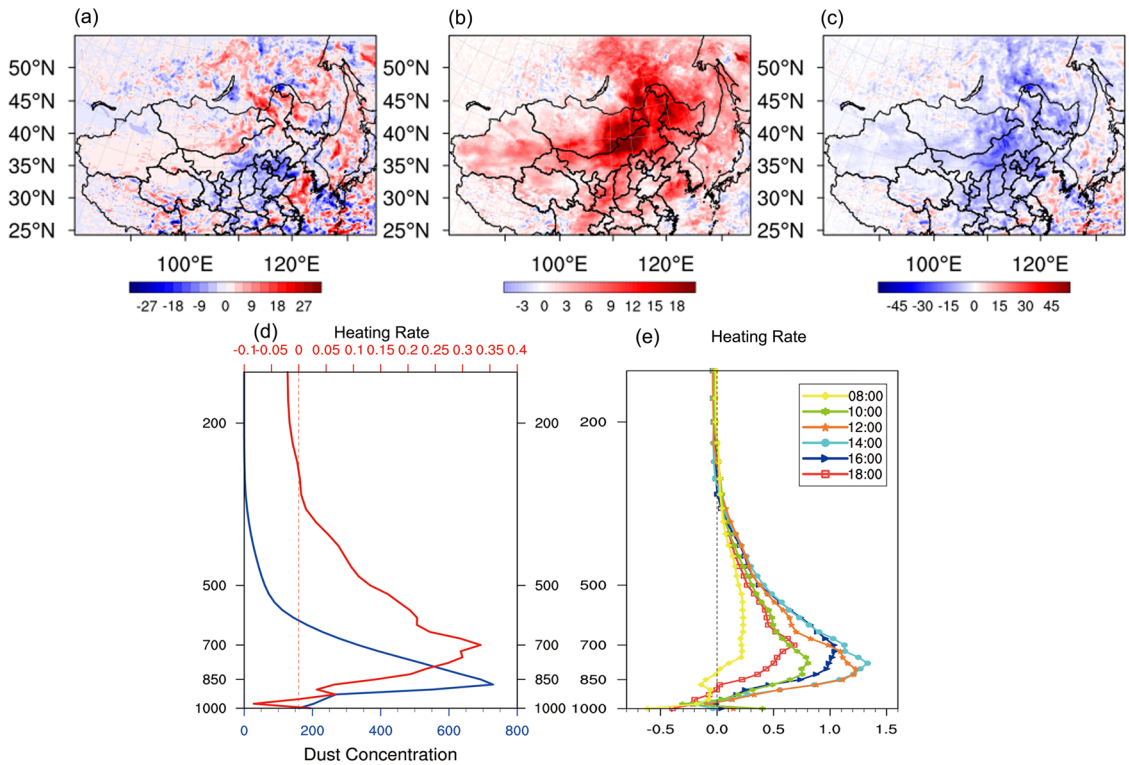

Fig. 3 Dust radiative forcing and dust-induced heating rate. Spatial distribution of dust net radiative forcing under all-sky (unit: W m^{-2}) (**a**) at the top of atmosphere, (**b**) in the atmosphere, and (**c**) at the bottom of atmosphere (color contour; unit: W m^{-2}). **d** Average vertical profiles for dust concentrations (blue solid line, unit: μg m^{-3}) and dust-induced changes in the heating rate (red solid line, unit: K day^{-1}). **e** Hourly heating rate (units: K day^{-1}) induced by dust radiative feedback in the study area (domain 2) during May 11–16, 2019. The results are based on the difference between the two parallel experiments.

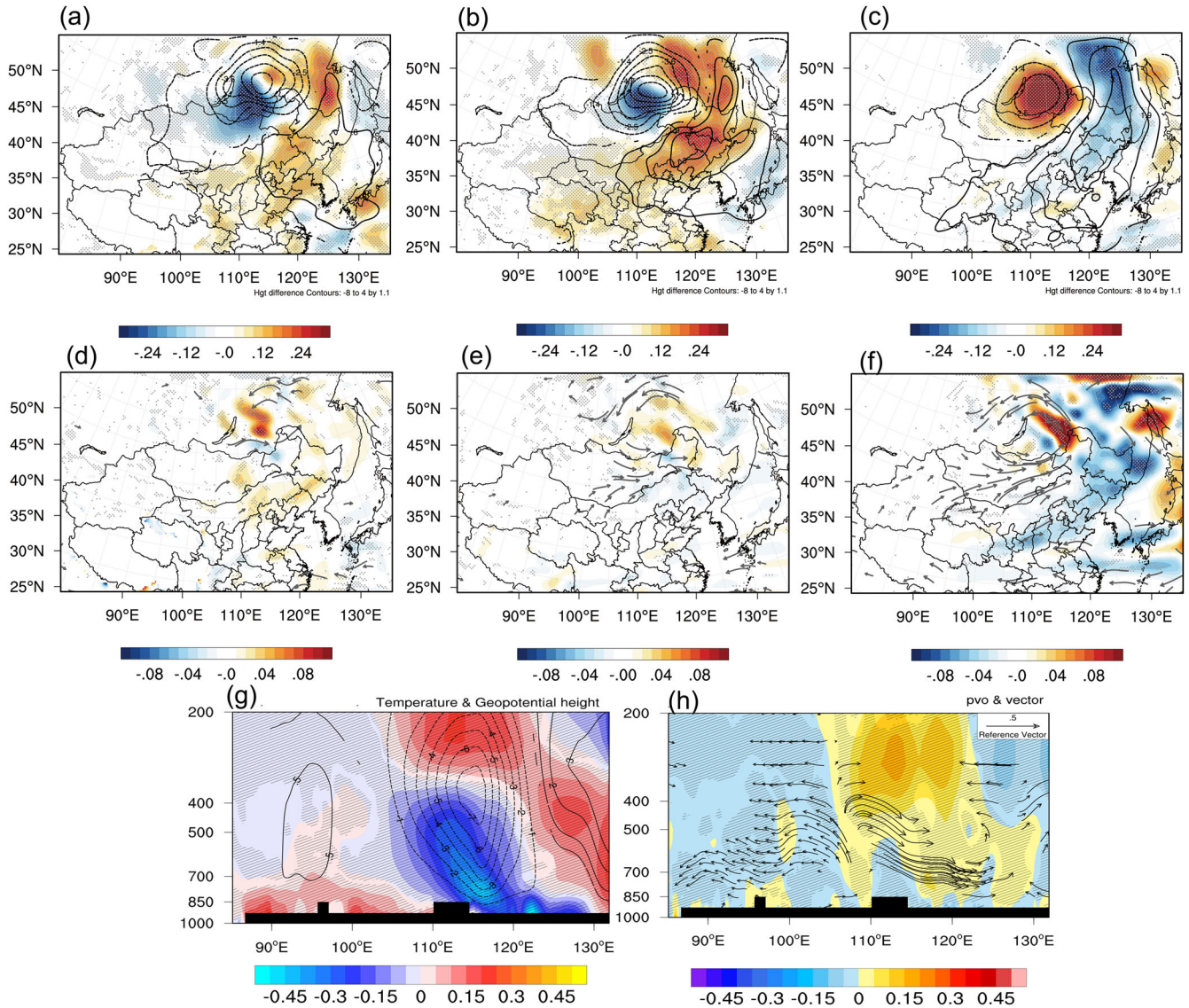

Fig. 4 Dust radiative feedback on enhancing Mongolian Cyclone. Spatial distribution of dust-induced temperature change (color contour; unit: °C) and geopotential height change (contour lines; unit: gpm) at (**a**) 700, (**b**) 500, and (**c**) 200 hPa and that of dust-induced potential vorticity (color contour; unit: PVU) and wind field (vectors; unit: m s^{-1}) at (**d**) 700, (**e**) 500, and (**f**) 200 hPa. Vertical cross sections of dust-induced latitudinal anomalies of (**g**) temperature (color contour; unit: °C) and geopotential height (contour lines; unit: gpm) as well as (**h**) potential vorticity (color contour; unit: PVU) and wind field (vectors; unit: m s^{-1}). The black dots and shadows represent statistical significance above the 90% level. The results are based on the difference between the two parallel experiments.

surface generally showed negative values (Fig. 3a, c). Atmospheric heating caused by dust exhibited considerable diurnal variation (Fig. 3e) and peaked at 1.22 K day^{-1} at 14:00 LT. Generally, dust aerosols change the dynamic structure by heating the atmosphere, and the enhanced wind speed enables more dust particles to be uplifted and transported, affording a positive feedback for dust transport.

Dust radiative feedback on the meteorological field (Fig. 4) facilitated the intensification of the Mongolian cyclone during the dust event and caused continuous accumulation of cold air in the middle and lower troposphere over northeast of Mongolia (Fig. 4a, b, c). The increase of low pressure always corresponds to the cold temperature anomaly, while the decrease of low pressure often corresponds to the warm temperature anomaly. Therefore, with increasing altitude, the low pressure gradually increased from 850 to 300 hPa, reaching maximum intensity near 300 hPa but gradually weakening above 300 hPa (Fig. 4g). The cold air accumulated at 700 hPa and 500 hPa (Fig. 4a, b) in this region also turned to warm ones at 200 hPa (Fig. 4c). Dust radiative feedback in the middle and low troposphere strengthens the zonal pressure and temperature gradient by enhancing the ridge of high pressure over northeast of China, intensifying the cold advection and Mongolian cyclone. In other words, dust radiative effect enhanced the temperature difference in the northeast of Mongolia, enhancing the geopotential height difference and cold advection, making the cyclone develop rapidly. Moreover, the wind field is also consistent with the variation in geopotential height field, which always presents cyclonic rotation in this region (Fig. 4d, e, f). The maximum potential vorticity induced by dust at 200 hPa exceeded 0.08 PVU. The potential vorticity decreases at 500 hPa and increases again at 700 hPa.

Mongolian cyclone can be continuously maintained and strengthened via dust radiative feedback. Dust vertical distribution plays a key role in weather and climate effects[42]. To clarify the influence of dust radiative feedback on the temperature and pressure vertical structure (Fig. 4g), we analyzed the latitudinal

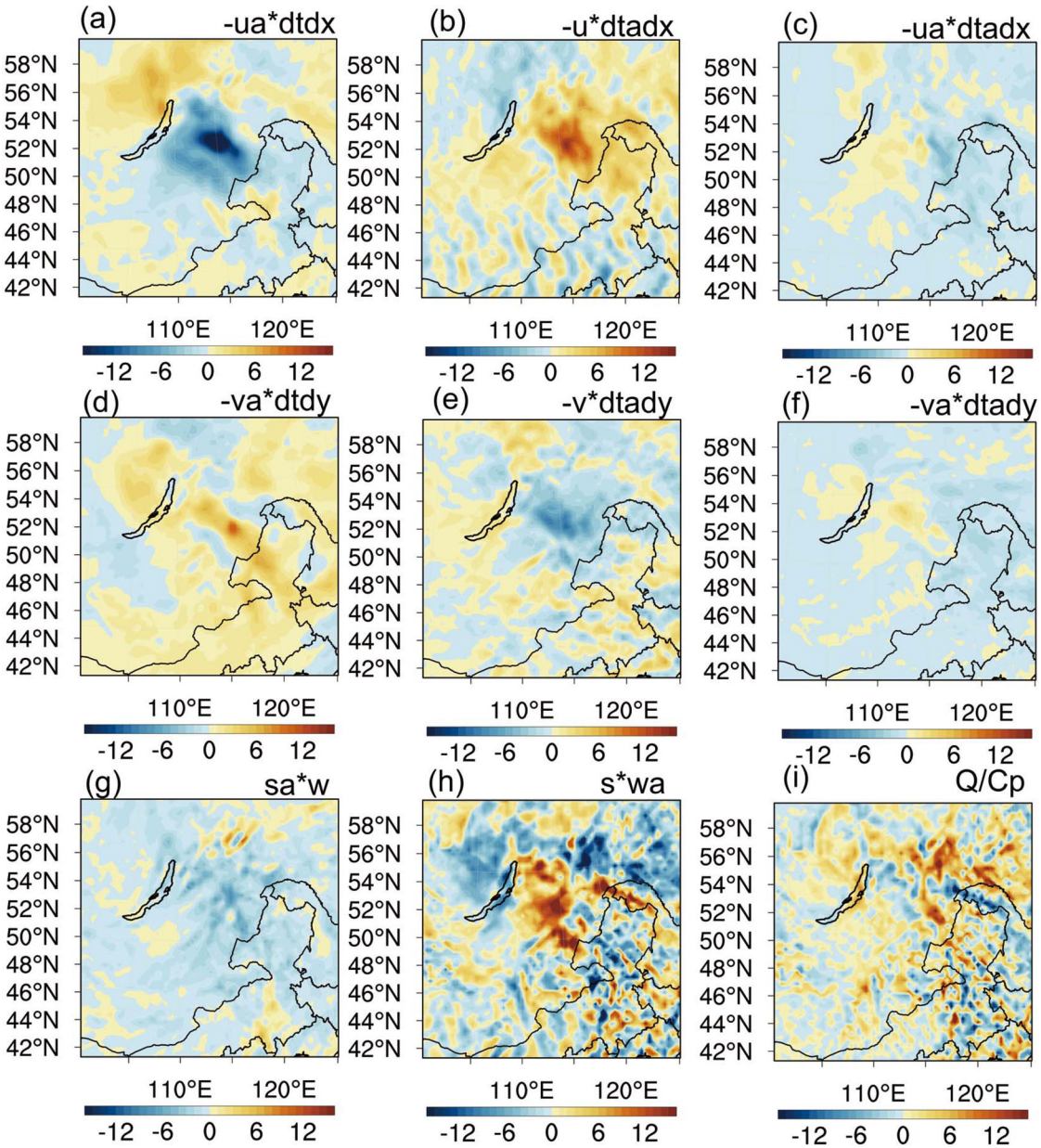

Fig. 5 Dust radiative feedback on the nine terms in the thermodynamic equation. Spatial distributions of nine terms (units: 10^{-2}) of the thermodynamic equation (Eq. 10) in the enhanced Mongolian cyclone area: (**a**) $-U'(\frac{\partial \overline{T}}{\partial x})$, (**b**) $-\overline{U}(\frac{\partial T'}{\partial x})$, (**c**) $-U'(\frac{\partial T'}{\partial x})$, (**d**) $-V'(\frac{\partial \overline{T}}{\partial y})$, (**e**) $-\overline{V}(\frac{\partial T'}{\partial y})$, (**f**) $-V'(\frac{\partial T'}{\partial y})$, (**g**) $\sigma'\overline{\omega}$, (**h**) $\overline{\sigma\omega}'$ and (**i**) $\frac{\Delta Q}{Cp}$.

anomalies section in the main cold air accumulation area (domain 1 in Supplementary Fig. 1). As shown in Fig. 4g, the colder air forms a wedge shape and descends deeply into the bottom of the warmer air, causing the warmer air to ascend along the colder ones. In the middle and back parts of the Mongolian cyclone, stable atmospheric structures were present with abundant colder (warmer) air accumulation in the lower (higher) layers. However, the front part of cyclone presented an opposite structure, with warmer (colder) air at lower (higher) altitudes. The development of the Mongolian cyclone was strengthened by the unstable and stable atmospheres present at the front and rear of the cyclone, respectively. Other's research[43] also support our results. It is reported that downward transfer of momentum from high altitudes is beneficial for intensifying Mongolian cyclone[44]. In the present study, the potential vorticity was maximum near 200 hPa and decreased at lower pressures (Fig. 4d, e, f). The cross section of the potential vortex with regional latitudinal anomalies shows that the maximum potential vortex (0.2 PVU) (where $1\text{PVU} = 1.0 \times 10^{-6}\ \text{m}^2\ \text{s}^{-1}\ \text{K}\ \text{kg}^{-1}$) near 200 hPa experiences downward transfer of momentum under the action of the wind field (Fig. 4h). Therefore, the cyclone over northeast of Mongolia was strengthened.

We then used the thermodynamic equation to explore the reason for the continuous cold air accumulation in the middle and lower troposphere over northeast of Mongolia. The influence of dust radiative feedback on the cold air over this region originated mainly from the zonal wind (Fig. 5a) and zonal temperature gradient (Fig. 5e). When the zonal wind field was enhanced, dust radiative feedback increased the transport of atmospheric cold advection over Siberia, thus cooling the atmosphere over northeast of Mongolia. However, the disturbance of vertical atmospheric movement caused by the dust radiative feedback

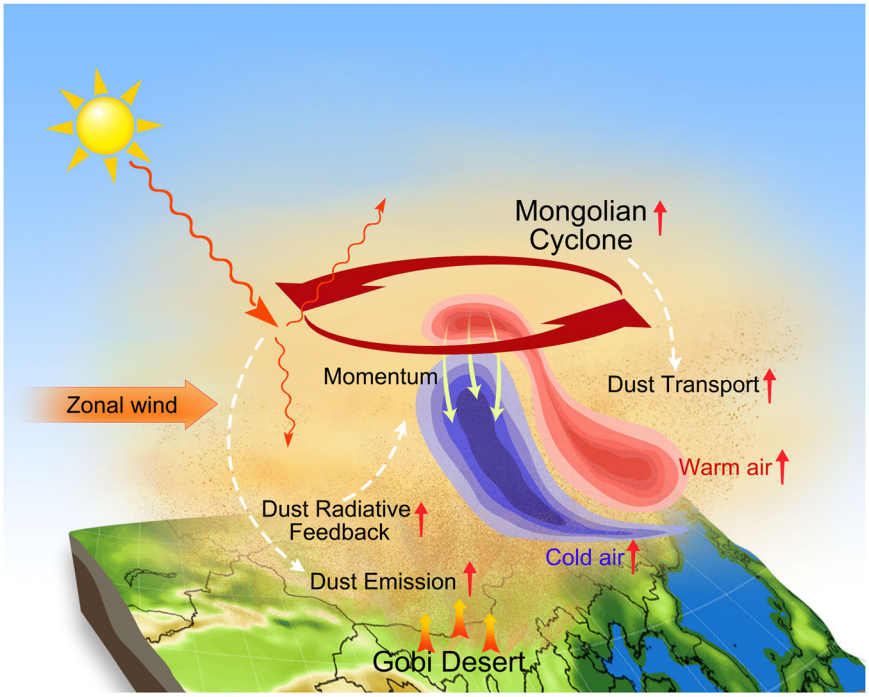

Fig. 6 Dust radiative feedback influence mechanism. Influence mechanism of dust radiative feedback over the GD on Mongolian cyclone intensification.

inhibited atmospheric cooling (Fig. 5h), which generally balances the thermodynamic equation. Dust radiative feedback yielded cyclone intensification over northeast of Mongolia, where atmospheric cooling and geopotential height reduction strengthened all layers of the cyclone. The strengthening of Mongolian cyclone further enhanced the upper westerly jets, forming a positive feedback process. This caused the GD dust aerosols to continue eastward transport, thus affecting northern China.

DISCUSSION

Based on two parallel experiments, the synoptic-scale effects of dust radiative forcing could be further explored. The effects of dust radiative feedback on the development and maintenance of Mongolian cyclone during a major dust event that occurred in May 2019 were investigated based on the dynamic dust sources coupled with the WRF-Chem model. Results showed that dust originating from the GD played a dominant role in the dust contribution over northern China. The intense Mongolian cyclone is responsible for the dust emission over the GD. With the influence of Mongolian cyclone, the GD dust continues to affect the downstream regions through westerly jets and is transported to northeast of Mongolia via southerlies. Dust radiative feedback shows a strong positive feedback on Mongolian Cyclone. By affecting zonal wind and temperature advection, the atmospheric cold anomaly in this region is enhanced. The intensified Mongolian cyclone is also sustained by enhancing the downward transmission of the high-level momentum of ~0.2 PVU and changing the stable atmospheric structure. After the Mongolian cyclone strengthened, westerly jets on its south side prevail and the GD dust is continuously transported to the downstream areas, causing higher dust concentrations in northern China (Fig. 6).

Driven by the increase dust in Asia and North Africa, the global dust mass loading has increased 55 ± 30% since pre-industrial times[45]. Dust radiative feedback has recently attracted considerable scientific attention as it could change the atmospheric thermal structure, which in turn can affect the weather and climate change[41,46]. Dust aerosols influence the radiation budget of the Earth by absorption, scatting of the longwave and shortwave radiation[47]. The dust radiation effect greatly reduces the temperature deviation between the surface and the atmosphere[48]. The atmospheric heating rate increased with dust radiative effect, resulting an increase of about 0.2 K in the middle troposphere (about 600 hPa)[49]. Dust radiative effect can further affect circulation and weather and climate change by influencing the atmospheric thermal structure. Previous studies on dust radiative feedback mainly focused on changes in meteorological elements on the surface over dust source areas, such as the effect of dust radiative feedback on reducing near-surface wind speed and surface temperature[50,51]. Such studies form a foundation for the basic research on dust radiative feedback. Herein, we investigate the dust radiative feedback over the GD on the weather and climate effects of an intensified cyclone in northeast of Mongolia. In addition, strengthening of the cyclone facilitates further eastward transmission of dust aerosols over the GD.

As an important dust source in East Asia, the GD is the main contributor to air pollution in northern China[28]. The results of the present study indicate that dust radiative feedback over the GD can intensify Mongolian cyclone. The participation of dynamic sources in actual analysis resolves the poor dust simulation of numerical models in the Mongolian Plateau. However, owing to the uncertainty of emission inventory and the deficiency of numerical simulation in this area, the linkage between dust radiative feedback in the GD and Mongolian cyclone is worthy of further exploration in the future.

METHODS

Model configuration and sensitivity simulations

To study the impact of dust aerosols on meteorology in China based on aerosol–meteorological interaction, a new-generation regional air quality model WRF-Chem[52] coupled with an online meteorological and chemical model was used to simulate a severe dust event occurred in northern China in May 2019. WRF-Chem is a public model developed by National Center for Atmospheric Research and National Oceanic and Atmospheric Administration.

Various physical and chemical processes including transport, wet and dry deposition, gas chemistry, radiation, and photolysis are considered in WRF-Chem, which has advantages in the numerical pollution simulation.

The meteorological initial fields of the WRF-Chem model were provided by the National Centers for Environmental Prediction final reanalysis data (NCEP/FNL) with a time interval of 6 h and a resolution of 1° × 1°. Related data of boundary conditions in the numerical simulation were output from the Community Atmosphere Model with Chemistry (CAM–Chem) model. The anthropogenic emission inventory was obtained from Emission Database for Global Atmospheric Research–Hemisphere Transport of Air Pollution (EDGAR–HTAP) global inventory at a horizontal resolution of 0.1° × 0.1° for 2010. EDGAR–HTAP provides specific inventory information for CH_4, CO, SO_2, NO_X, nonmethane volatile organic compounds (NMVOCs), NH_3, PM_{10}, $PM_{2.5}$, black carbon (BC), and organic carbon (OC). Biomass emission data were obtained from Model of Emission of Gases and Aerosol from Nature (MEGAN). Other detailed physical parameterization schemes used in this study are shown in Table 1.

WRF-Chem model version 3.9.1 was adopted with Lambert projection and a one-way nested grid. This study used 42°N and 108°E as the center grid, with a spatial resolution of 151 × 191 grid points and a grid resolution of 30 km. Study areas included the TD and GD, which are the main dust source areas in China. Simulation period is 00:00 UTC May 10 to 00:00 UTC May 31, 2019, with the first day used as the spin-up period. The severe dust event occurred from May 11 to May 16, 2019, was selected as the main study period. The main simulation domain is displayed in Supplementary Fig. 1. Dust aerosol is mainly activated by GOCART dust emission scheme in the WRF-Chem. When the dust emission scheme is turned off, dust aerosol is also removed in the modeling. To investigate the feedback between dust-radiation interaction and meteorology, we conducted two parallel experiments with and without dust emission in the study. Two simulations that are respectively, designated as "EXP_CTRL" and "EXP_NODE" are carried out. The EXP_CTRL experiment is defined as a control simulation in which dust emission scheme is turned on and dust aerosols are allowed to provide it's feedback to the radiation. The sensitivity experiment ("EXP_NODE") is conducted by closing dust emission scheme and the direct and indirect feedback between dust aerosol and the radiation scheme. The difference between control and sensitivity result are considered as the synoptic-scale effects of dust radiative forcing[53,54]. This method is also widely used to explore the radiative forcing of different kinds of aerosol and its effects on meteorological fields[55–57].

Dynamic dust source

To effectively describe dust emission, this study adopted the Georgia Tech/Goddard Global Ozone Chemistry Aerosol Radiation and Transport (GOCART) scheme, in which the dust emission flux (F) is calculated using the following formula:

$$F = CSs_p u_{10m}^2 (u_{10m} - u_t)(u_{10m} \geq u_t), \quad (1)$$

where C denotes the constant of the empirical derivation function, S is the source function of soil wind erosion, s_p represents the fraction of each size bin in erodible dust, u_{10m} denotes the horizontal wind speed at 10 m, and u_t represents the threshold velocity of particle size, air density and soil moisture. More details about the coupling of the GOCART scheme with the WRF-Chem model can be found in Zhao et al. [58]. When GOCART scheme is turned off, dust aerosol is removed in the modeling.

Traditional numerical models treat the potential dust source as static climatic distribution and ignore its dynamic activity, causing considerable uncertainty in the difference in seasonal dust emissions[59]. Dust sources used in previous GOCART simulations were based on average land covers from the Advanced Very High Resolution Radiometer (AVHRR) satellite, which has no temporal variance[60]. Therefore, a global-scale dynamic dust source has been developed using time-varying NDVI data[61,62]. The dust source function (S) is determined by surface bareness (B) and topographic features (H)[61,62]. Topographic differences are closely related to dust accumulation[63]. H represents the topographic differences in the grid relative to the surroundings, as shown in Eq. (2), where the lower H is, the easier the dust is to accumulate.

$$H = \left(\frac{Z_{\max} - Z_i}{Z_{\max} - Z_{\min}}\right)^5. \quad (2)$$

In this equation, Z represents the terrain elevation in the grid, Z_{max} and Z_{min} correspond to the highest and lowest points in the surrounding areas (calculated grids) of the 10° × 10°, respectively, and Z_i denotes the height of grid i. Power of 5 is used to improve the terrain contrast. Bare soil is indicated when the normalized difference vegetation index (NDVI) is <0.17 in each grid. Therefore, the surface bareness is calculated using the ratio of grid numbers below 0.17 ($N_{<0.17}$) to the total grid number N_{total}:

$$B = \frac{N_{<0.17}}{N_{total}}. \quad (3)$$

However, the dynamic dust source function based on this calculation method is not accurate and the regions with perennial ice and snow cover at high latitudes also showing dust source function maximum. We also employed land cover from MODIS to constrain the calculated S to reproduce the spatial distribution of dust sources. Therefore, a global-scale dynamic dust source has been developed[61,62].

Table 1. WRF-Chem configuration options for physical and chemical parameterizations.

Physical and chemical processes	Configuration
Microphysics	Thompson[77]
Long/shortwave radiation	RRTMG[78]
Land surface model	Noah[79]
Boundary layer scheme	YSU[80]
Cumulus parameterization	Grell-Freitas[81]
Dust emission estimation	GOCART[82]
Aerosol chemistry	MOZART Chemistry and GOCART

Aerosol optical depth

The WRF-Chem can effectively simulate aerosol optical depth, which is vertically derived from the accumulation of the extinction coefficient. The aerosol extinction coefficient is determined by the following formula[64,65]:

$$b_{ext}(\lambda, X) = \sum_{i=1}^{i=m} Q_e(x_i, X)\pi r_i^2 n(r_i, X) \quad (4)$$

where Q_e shows the exctinction efficiency, r_i is the wet radius, x_i is the size parameter, and $n(r_i, X)$ is the number concentration (number per unit volume) associated with the section "i".

AOD mainly depends on particle size distribution, composition, mixing state and hygroscopic property, and is calculated according to aerosol concentrations and aerosol optical properties[66,67]. It was obtained from WRF-Chem by vertical integration (from the ground to the top of the domain) of the aerosol extinction at 550 nm, which was obtained as the output of the

WRF-Chem[68].

$$AOD = \int_0^{\infty} b_{ext}(z)dz \tag{5}$$

Aerosol radiative forcing

Direct radiative forcing of aerosols refers to radiation change caused by scattering and absorption. That is, direct radiative forcing of dust can be defined as the difference between the net radiative flux with and without dust, whereas atmospheric radiative flux refers to the radiative energy passing through any surface per unit time. Downward and upward radiation fluxes are characterized by positive and negative values, respectively. As calculated using the following equations, dust radiative forcing is always estimated at the TOA, in the atmosphere (ATM), and at the bottom of the atmosphere (BOA):

$$DRF_{ATM} = NF_{ATM}^{with} - NF_{ATM}^{no}, \tag{6}$$

$$DRF_{TOA} = NF_{TOA}^{with} - NF_{TOA}^{no}, \tag{7}$$

$$DRF_{BOA} = NF_{BOA}^{with} - NF_{BOA}^{no}, \tag{8}$$

$$NF = NF_{\downarrow} - NF_{\uparrow}, \tag{9}$$

where DRF represents direct radiative forcing and NF indicates the net radiative flux[69–71].

Thermodynamic equations

The following thermodynamic equation were used to accurately evaluate the effect of dust radiative feedback on thermal structure in the meteorological field. We defined the experiment in EXP_NODE as the mean quantity in thermodynamic equation, and the difference between the two parallel experiments was considered as disturbance. In the actual analysis, each terms in the following equation were integrated from the surface to 300 hPa.

$$\int_{Ps}^{p0}\left\{\underbrace{-U'\left(\frac{\partial\overline{T}}{\partial x}\right)-\overline{U}\left(\frac{\partial T'}{\partial x}\right)-U'\left(\frac{\partial T'}{\partial x}\right)-V'\left(\frac{\partial\overline{T}}{\partial y}\right)-\overline{V}\left(\frac{\partial T'}{\partial y}\right)-V'\left(\frac{\partial T'}{\partial y}\right)+\sigma'\overline{\omega}+\overline{\sigma}\omega'}_{(adiabatic\ change)}+\underbrace{\frac{\Delta Q}{Cp}}_{(nonadiabatic\ change)}\right\}\frac{dp}{g}=0 \tag{10}$$

The atmospheric apparent heat source Q1 is calculated using an inverse algorithm based on the thermodynamic equation[72]:

$$Q1 = C_p\frac{\partial T}{\partial t} - C_p(\omega\sigma - V\cdot\nabla T). \tag{11}$$

Data

The MODIS cloud image provides effective records about the frequency and distribution of cloud. It can be obtained from the online website in png format. As a vital sensor onboard Terra and Aqua, the Moderate Resolution Imaging Spectroradiometer (MODIS) provides reliable global information on clouds, aerosols, land cover, and other parameters[73] and always plays an important role in module evaluation. Its AOD products are at a wavelength of 550 nm with dark target and deep blue algorithms (MOD08 and MYD08) and contain daily degree grid average values of atmospheric parameters at a resolution of 1° × 1°. The aerosol index (AI) derived from Aura Ozone Monitoring Instrument (OMI) covers the period 2004–2023 and exhibits a horizontal resolution of 1° × 1°. The AI is extremely sensitive to ultraviolet (UV)-absorbing aerosols, such as smoke, mineral dust, and volcanic ash[74]. OMI is the successor to the total ozone mapping spectrometer (TOMS) instrument for monitoring ozone levels, air quality, and climate of the earth[75]. Moreover, the daily aerosol ground observations at sites are derived using the Aerosol Robotic Network (AERONET), which is a wide network of sun photometers located worldwide[76].

DATA AVAILABILITY

Modis dataset were obtained from https://modis.gsfc.nasa.gov/. MODIS cloud image is provided in https://wvs.earthdata.nasa.gov/. AERONET data are available through https://aeronet.gsfc.nasa.gov/. FNL reanalysis data are accessed from http://dss.ucar.edu/datasets/. Cam-chem data were used from https://www.acom.ucar.edu/cam-chem/cam-chem.shtml.

CODE AVAILABILITY

The NCL codes used to run the analysis can be obtained upon request to the corresponding authors.

Received: 2 January 2023; Accepted: 3 July 2023;
Published online: 14 July 2023

REFERENCES

1. Kinne, S. et al. An AeroCom initial assessment – optical properties in aerosol component modules of global models. *Atmos. Chem. Phys.* **6**, 1815–1834 (2006).
2. Tegen, I., Lacis, A. & Fung, I. The influence on climate forcing of mineral aerosols from disturbed soils. *Nature* **380**, 419–422 (1996).
3. Ramanathan, V., Crutzen, P. J., Kiehl, J. T. & Rosenfeld, D. Aerosols, climate, and the hydrological cycle. *Science* **294**, 2119–2124 (2001).
4. Huang, J. et al. Taklimakan dust aerosol radiative heating derived from CALIPSO observations using the Fu-Liou radiation model with CERES constraints. *Atmos. Chem. Phys.* **9**, 4011–4021 (2009).
5. Qian, Y. et al. Heavy pollution suppresses light rain in China: observations and modeling. *J. Geophys. Res. Atmos.* **114**, D00K02 (2009).
6. Ariya, P. A. & Amyot, M. New directions: the role of bioaerosols in atmospheric chemistry and physics. *Atmos. Environ.* **38**, 1231–1232 (2004).
7. Švédová, B. et al. Water-soluble ions in dust particles depending on meteorological conditions in urban environment. *J. Environ. Manag.* **237**, 322–331 (2019).
8. Kasimov, N. S., Vlasov, D. V. & Kosheleva, N. E. Enrichment of road dust particles and adjacent environments with metals and metalloids in eastern Moscow. *Urban Clim.* **32**, 100638 (2020).
9. Zhao, H. J. et al. Characteristics of visibility and particulate matter (PM) in an urban area of Northeast China. *Atmos. Pollut. Res.* **4**, 427–434 (2013).
10. Che, H. Z. et al. Haze trends over the capital cities of 31 provinces in China, 1981–2005. *Theor. Appl Climatol.* **97**, 235–242 (2009).
11. Ma, X. Y., Jia, H. L., Sha, T., An, J. L. & Tian, R. Spatial and seasonal characteristics of particulate matter and gaseous pollution in China: Implications for control policy. *Environ. Pollut.* **248**, 421–428 (2019).
12. Jickells, T. D. et al. Global iron connections between desert dust, ocean biogeochemistry, and climate. *Science* **308**, 67–71 (2005).
13. Pabortsava, K. et al. Carbon sequestration in the deep Atlantic enhanced by Saharan dust. *Nat. Geosci.* **10**, 189–194 (2017).
14. Ding, A. J. et al. Intense atmospheric pollution modifies weather: a case of mixed biomass burning with fossil fuel combustion pollution in eastern China. *Atmos. Chem. Phys.* **13**, 10545–10554 (2013).
15. Chen, Y. et al. The role of boundary layer height in India on transboundary pollutions to the Tibetan Plateau. *Sci. Total Environ.* **837**, 155816 (2022).
16. Zhang, C. X. et al. Satellite UV-Vis spectroscopy: implications for air quality trends and their driving forces in China during 2005–2017. *Light Sci. Appl.* **8**, 100 (2019).
17. Wang, Z. et al. Elevated dust layers inhibit dissipation of heavy anthropogenic surface air pollution. *Atmos. Chem. Phys.* **20**, 14917–14932 (2020).
18. Chen, S. Y. et al. Emission, transport, and radiative effects of mineral dust from the Taklimakan and Gobi deserts: comparison of measurements and model results. *Atmos. Chem. Phys.* **17**, 2401–2421 (2017).
19. Heinold, B., Tegen, I., Schepanski, K. & Hellmuth, O. Dust radiative feedback on Saharan boundary layer dynamics and dust mobilization. *Geophys. Res. Lett.* **35**, L20817 (2008).

20. Yang, Y. et al. Dust-wind interactions can intensify aerosol pollution over eastern China. *Nat. Commun.* **8**, 15333 (2017).
21. Ahn, H. J., Park, S. U. & Chang, L. S. Effect of direct radiative forcing of Asian dust on the meteorological fields in East Asia during an Asian dust event period. *J. Appl Meteorol. Climatol.* **46**, 1655–1681 (2007).
22. Sun, J. M., Zhang, M. Y. & Liu, T. S. Spatial and temporal characteristics of dust storms in China and its surrounding regions, 1960–1999: relations to source area and climate. *J. Geophys. Res. Atmos.* **106**, 325–10,334 (2001).
23. Qian, W. H., Quan, L. S. & Shi, S. Y. Variations of the dust storm in China and its climatic Control. *J. Clim.* **15**, 1216–1229 (2002).
24. Wang, X., Huang, J. P., Ji, M. X. & Higuchi, K. Variability of East Asia dust events and their long-term trend. *Atmos. Environ.* **42**, 3156–3165 (2008).
25. Li, X. L. & Zhang, H. R. Research on threshold friction velocities during dust events over the Gobi Desert in northwest China. *J. Geophys. Res. Atmos.* **116**, D20210 (2011).
26. Zong, Q. et al. Changes in dust activity in spring over East Asia under a global warming scenario. *Asia-Pac. J. Atmos. Sci.* **57**, 839–850 (2021).
27. Bao, T., Gao, T., Nandintsetseg, B., Yong, M. & Jin, E. Variations in frequency and intensity of dust events crossing the Mongolia-China border. *SOLA* **17**, 145–150 (2021).
28. Chen, S. Y. et al. Comparison of dust emissions, transport, and deposition between the Taklimakan Desert and Gobi Desert from 2007 to 2011. *Sci. China Earth Sci.* **60**, 1338–1355 (2017).
29. Huang, J. P. et al. Long-range transport and vertical structure of Asian dust from CALIPSO and surface measurements during PACDEX. *J. Geophys. Res. Atmos.* **113**, D23212 (2008).
30. Liu, L. et al. Contrasting influence of Gobi and Taklimakan deserts on the dust aerosols in western North America. *Geophys. Res. Lett.* **46**, 9064–9071 (2019).
31. Zhao, L. N. & Zhao, S. X. Diagnosis and simulation of a rapidly developing cyclone related to a severe dust storm in East Asia. *Glob. Planet Change* **52**, 105–120 (2006).
32. Zhao, T. L., Gong, S. L., Zhang, X. Y. & Jaffe, A. Asian dust storm influence on North American ambient PM levels: observational evidence and controlling factors. *Atmos. Chem. Phys.* **8**, 2717–2728 (2008).
33. Lee, Y. C. et al. Dust episodes in Hong Kong (South China) and their relationship with the Sharav and Mongolian cyclones and jet streams. *Air Qual. Atmos. Health* **5**, 413–424 (2012).
34. Uematsu, M. et al. Transport of mineral aerosol from Asia over the North Pacific ocean. *J. Geophys. Res. Atmos.* **88**, 5343–5352 (1983).
35. Murayama, T. et al. Ground-based network observation of Asian dust events of April 1998 in east Asia. *J. Geophys. Res. Atmos.* **106**, 1834–18359 (2001).
36. Wang, Y. Y. & Wang, M. Z. The strongest sandstorm weather since spring occurred in some areas of Inner Mongolia. Youthzqw. https://baijiahao.baidu.com/s?id=1633388768605212203&wfr=spider&for=pc,2019-05-13 (2019).
37. Herman, J. R. et al. Global distribution of UV-absorbing aerosols from Nimbus 7/TOMS data. *J. Geophys. Res. Atmos.* **102**, 16911–16922 (1997).
38. Al-Zuhairi, M. F. & Kadhum, J. H. Spatiotemporal distribution of the Aura-OMI aerosol index and dust storm case studies over Iraq. *Arab J. Geosci.* **14**, 909 (2021).
39. Das, S., Dey, S., Dash, S. K., Giuliani, G. & Solmon, F. Dust aerosol feedback on the Indian summer monsoon: sensitivity to absorption property. *J. Geophys. Res. Atmos.* **120**, 9642–9652 (2015).
40. Chen, S. Y. et al. Sources, characteristics and climate impact of light-absorbing aerosols over the Tibetan Plateau. *Earth Sci. Rev.* **232**, 104111 (2022).
41. Xie, X. et al. Radiative feedbacks of dust in snow over eastern Asia in CAM4-BAM. *Atmos. Chem. Phys.* **18**, 12683–12698 (2018).
42. Liu, D. et al. Vertical structures of dust aerosols over East Asia Based on CALIPSO retrievals. *Remote Sens* **11**, 701 (2019).
43. Xun, X. Y., Jiang, X. G. & Wu, X. H. *A numerical simulation study of surface heat flux influence on Mongolia cyclone*. A compilation of Papers of the 8th National Outstanding Young Meteorological Scientists Symposium. 571–584 (in Chinese) (2014).
44. Uccellini, L. W., Keyser, D., Brill, K. F. & Wash, C. H. The presidents' day cyclone of 18–19 February 1979: influence of upstream trough amplification and associated tropopause folding on rapid cyclogenesis. *Mon. Weather Rev.* **113**, 962–988 (1985).
45. Kok, J. F. et al. Mineral dust aerosol impacts on global climate and climate change. *Nat. Rev. Earth Environ.* **4**, 71–86 (2023).
46. Zhao, D. et al. Influence of dust aerosols on snow cover over the Tibetan plateau. *Front Environ. Sci.* **10**, 839691 (2022).
47. Ackerman, S. A. & Chung, H. Radiative effects of airborne dust on regional energy budgets at the top of the atmosphere. *J. Appl. Meteorol.* **31**, 223–233 (1992).
48. Li, H. Q. & Wang, C. H. Impact of dust radiation effect on simulations of temperature and wind – a case study in Taklimakan desert. *Atmos. Res.* **273**, 106163 (2022).
49. Spyrou, C., Kallos, G. & Mitsakou, C. Radiative effects of desert dust on weather and regional climate. *Atmos. Chem. Phys.* **13**, 5489–5504 (2013).
50. Han, Z. W., Li, J. W., Guo, W. D., Xiong, Z. & Zhang, W. A study of dust radiative feedback on dust cycle and meteorology over East Asia by a coupled regional climate-chemistry-aerosol model. *Atmos. Environ.* **68**, 54–63 (2013).
51. Ma, X. Y. & Yu, F. Q. Effect of spectral-dependent surface albedo on Saharan dust direct radiative forcing. *Geophys. Res. Lett.* **39**, L09808 (2012).
52. Grell, G. A. et al. Fully coupled "online" chemistry within the WRF model. *Atmos. Environ.* **39**, 6957–6975 (2005).
53. Li, M. M. et al. Impacts of aerosol-radiation feedback on local air quality during a severe haze episode in Nanjing megacity, eastern China. *Tellus B Chem. Phys. Meteorol.* **69**, 1339548 (2017).
54. Huang, X. et al. Smoke-weather interaction affects extreme wildfires in diverse coastal regions. *Science* **379**, 457–461 (2023).
55. Roberts, D. L. & Jones, A. Climate sensitivity to black carbon aerosol from fossil fuel combustion. *J. Geophys. Res. Atmos.* **109**, D16202 (2004).
56. Matsui, H., Hamilton, D. S. & Mahowald, N. M. Black carbon radiative effects highly sensitive to emitted particle size when resolving mixing-state diversity. *Nat. Commun.* **9**, 3446 (2018).
57. Chen, X. T., Kang, S. C., Yang, J. H. & Ji, Z. M. Investigation of black carbon climate effects in the Arctic in winter and spring. *Sci. Total Environ.* **751**, 142145 (2021).
58. Zhao, C. et al. The spatial distribution of mineral dust and its shortwave radiative forcing over North Africa: modeling sensitivity to dust emissions and aerosol size treatments. *Atmos. Chem. Phys.* **10**, 8821–8838 (2010).
59. Xi, X. & Sokolik, I. N. Quantifying the anthropogenic dust emission from agricultural land use and desiccation of the aral sea in central asia. *J. Geophys. Res. Atmos.* **121**, 12270–12281 (2016).
60. DeFries, R. S. & Townshend, J. R. G. NDVI-derived land cover classification at a global scale. *Int. J. Remote Sens.* **15**, 3567–3586 (1994).
61. Kim, D. et al. The effect of the dynamic surface bareness on dust source function, emission, and distribution. *J. Geophys. Res. Atmos.* **118**, 871–886 (2013).
62. Kim, D. et al. Development of high-resolution dynamic dust source function - a case study with a strong dust storm in a regional model. *Atmos. Environ.* **159**, 11–25 (2017).
63. Ma, J. M. & Daggupaty, S. M. Effective dry deposition velocities for gases and particles over heterogeneous terrain. *J. Appl Meteorol.* **39**, 1379–1390 (2000).
64. Fast, J. D. et al. Evolution of ozone, particulates, and aerosol direct radiative forcing in the vicinity of Houston using a fully coupled meteorology-chemistry-aerosol model. *J. Geophys. Res. Atmos.* **111**, D21305 (2006).
65. Barnard, J. C., Fast, J. D., Paredes-Miranda, G., Arnott, W. P. & Laskin, A. Technical note: evaluation of the WRF-Chem "aerosol chemical to aerosol optical properties" module using data from the MILAGRO campaign. *Atmos. Chem. Phys.* **10**, 7325–7340 (2010).
66. Ukhov, A. et al. Assessment of natural and anthropogenic aerosol air pollution in the Middle East using MERRA-2, CAMS data assimilation products, and high-resolution WRF-Chem model simulations. *Atmos. Chem. Phys.* **20**, 9281–9310 (2020).
67. Yu, F., Luo, G. & Ma, X. Regional and global modeling of aerosol optical properties with a size, composition, and mixing state resolved particle microphysics model. *Atmos. Chem. Phys.* **12**, 5719–5736 (2012).
68. Karagulian, F. et al. Analysis of a severe dust storm and its impact on air quality conditions using WRF-Chem modeling, satellite imagery, and ground observations. *Air Qual. Atmos. Health* **12**, 453–470 (2019).
69. Moorthy, K. K., Babu, S. S. & Satheesh, S. K. Aerosol characteristics and radiative impacts over the Arabian Sea during the intermonsoon season: results from ARMEX field campaign. *J. Atmos. Sci.* **62**, 192–206 (2005).
70. Liu, X. et al. The influence of dusts on radiation and temperature over the eastern Asia with a regional climate model. *Sci. Total Environ.* **792**, 148351 (2021).
71. Zhang, X. et al. Direct radiative forcing induced by light-absorbing aerosols in different climate regions over East Asia. *J. Geophys. Res. Atmos.* **125**, e2019JD032228 (2020).
72. Yanai, M., Esbensen, S. & Chu, J. H. Determination of bulk properties of tropical cloud clusters from large-scale heat and moisture budgets. *J. Atmos. Sci.* **30**, 611–627 (1973).
73. Kaufman, Y. J. et al. Operational remote sensing of tropospheric aerosol over land from EOS moderate resolution imaging spectroradiometer. *J. Geophys. Res. Atmos.* **102**, 17051–17067 (1997).
74. Guan, H. et al. A multi-decadal history of biomass burning plume heights identified using aerosol index measurements. *Atmos. Chem. Phys.* **10**, 6461–6469 (2010).
75. Buchard, V. et al. Using the OMI aerosol index and absorption aerosol optical depth to evaluate the NASA MERRA Aerosol Reanalysis. *Atmos. Chem. Phys.* **15**, 5743–5760 (2015).
76. Rubin, J. L. et al. Assimilation of AERONET and MODIS AOT observations using variational and ensemble data assimilation methods and its impact on aerosol forecasting skill. *J. Geophys. Res. Atmos.* **122**, 4967–4992 (2017).
77. Thompson, G., Field, P. R., Rasmussen, R. M. & Hall, W. D. Explicit forecasts of winter precipitation using an improved bulk microphysics scheme. Part II:

Implementation of a new snow parameterization. *Mon. Weather Rev.* **136**, 5095–5115 (2008).
78. Lacono, M. J. et al. Radiative forcing by long-lived greenhouse gases: Calculations with the AER radiative transfer models. *J. Geophys. Res. Atmos.* **113**, D13103 (2008).
79. Tewari, M. et al. Implementation and verification of the unified NOAH land surface model in the WRF model. *20th conference on weather analysis and forecasting/16th conference on numerical weather prediction. 11–15 (2004).*
80. Hong, S. Y., Noh, Y. & Dudhia, J. A new vertical diffusion package with an explicit treatment of entrainment processes. *Mon. Weather Rev.* **134**, 2318–2341 (2006).
81. Grell, G. A. & Freitas, S. R. A scale and aerosol aware stochastic convective parameterization for weather and air quality modeling. *Atmos. Chem. Phys.* **14**, 5233–5250 (2014).
82. Ginoux, P. et al. Sources and distributions of dust aerosols simulated with the GOCART model. *J. Geophys. Res. Atmos.* **106**, 20255–20273 (2001).

ACKNOWLEDGEMENTS

This work was jointly supported by the Project supported by the Joint Fund of the National Natural Science Foundation of China and the China Meteorological Administration (Grant No. U2242209), the National Natural Science Foundation of China (Grant No. 42175106), China Postdoctoral Science Foundation (2020M681156) and Self-supporting Program of Guangzhou Laboratory (Grant No. SRPG22-007).

AUTHOR CONTRIBUTIONS

Y.C. conducted paper writing and data analysis. S.C. proposed and conceived the study. J.Z. participated in the thermodynamic equation analysis. Y.Z. constructed the dynamic dust source. S.C., D.Z., H.B, K.A., H.Y., Y.Y. and J.C. contributed to the discussion and paper writing. Y.C. prepared the manuscript with contribution from all the authors.

COMPETING INTERESTS

The authors declare no competing interests.

ADDITIONAL INFORMATION

Supplementary information The online version contains supplementary material available at https://doi.org/10.1038/s41612-023-00418-y.

Correspondence and requests for materials should be addressed to Siyu Chen.

Reprints and permission information is available at http://www.nature.com/reprints

Publisher's note Springer Nature remains neutral with regard to jurisdictional claims in published maps and institutional affiliations.